https://doi.org/10.5194/egusphere-2026-1422
Preprint. Discussion started: 11 May 2026

Research on deep learning-based missing echo restoration method for weather radar mosaic data

Husong Guo[1], Muyun Du[2], Xiangyu Fan[1,3], Cuihong Wu[2], Anwei Lai[2], Hedi Ma[2]

[1]School of Information Science and Engineering, University of Jinan, Jinan 250022, China

[2]Heavy Rainfall Research Center of China/China Meteorological Administration Basin Heavy Rainfall Key Laboratory/Hubei Key Laboratory for Heavy Rain Monitoring and Warning Research, Institute of Heavy Rain, China Meteorological Administration, Wuhan 430205, China

[3]School of Biological Science and Technology, University of Jinan, Jinan 250022, China

Correspondence to: Muyun Du (dumy@whihr.com.cn)

Abstract. Radar mosaic data represent a critical and widely utilized resource in weather forecasting. Nevertheless, the frequent occurrence of regional radar echo gaps, caused by factors including radar hardware malfunctions, data delivery delays, and software processing errors—each contributing to substantial spatial uncertainty in the missing areas—significantly constrains its quantitative application. To address this issue, we propose BiConvLSTM-UNet, a sequence reconstruction model designed to restore missing radar echoes. The model operates without relying on a missing-value mask during both training and inference, learning the inherent spatiotemporal variation patterns of radar echoes to reconstruct complete sequences. A post-processing procedure is implemented to minimize the impact of reconstruction on areas without missing data. Furthermore, multiple missing scenarios are synthetically generated to improve the model's robustness and repair performance across diverse missing-data conditions. Comparative assessments against traditional and other deep learning approaches demonstrate the superior inpainting performance of the proposed BiConvLSTM-UNet across multiple missing-data scenarios. The method introduces minimal artifact to non-missing regions, and subsequent post-processing further diminishes reconstruction errors. Moreover, the model sustains consistent performance across varying missing data lengths and continuity patterns, indicating robust generalization capabilities. Consequently, the BiConvLSTM-UNet is more adept at addressing the intricate and varied scenarios of incomplete radar mosaic data encountered in practical applications.

1 Introduction

Weather radar, as a meteorological detection equipment with excellent technical performance, plays an important role in key areas such as early warning and forecasting of severe convective weather (Esbrí et al., 2023; Yao et al., 2026), disaster prevention and mitigation (Forcadell et al., 2024), aviation safety assurance and artificial weather modification

https://doi.org/10.5194/egusphere-2026-1422
Preprint. Discussion started: 11 May 2026

operations (Fabry, 2015; Liu et al., 2024). However, the detection range of a single radar is limited (effective radius of about 200-300 km), and there are terrain obstructions and blind spots, making it difficult to meet the needs of continuous monitoring of large-scale weather systems. To this end, radar mosaic data generated by integrating observation data from multiple radars through network fusion technology has broken through the limitation of the detection range of a single radar and can effectively support large-scale tracking and early warning of severe weather (Saltikoff et al., 2019). However, radar hardware failure, file arrival delays, program execution errors and other reasons often lead to regional data loss in radar mosaic data, which seriously limits its quantitative application (Li et al., 2025; Yin et al., 2022; Zhao et al., 2025).

To address the issue of missing radar data, researchers have explored a variety of approaches. Zhang et al. (2013) exploited the insensitivity of the total differential phase (Φ_{DP}) of dual-polarization radar to partial beam blocking (PBB) (Gou and Chen, 2021). Based on the K_{DP}–Z power-law relationship, they dynamically estimated the beam blocking fraction (BBF) through integration along the radar beam, thereby enabling quantitative correction of blockage effects caused by terrain, buildings, and vegetation, as well as reflectivity reconstruction. In addition, optical flow methods (Peng et al., 2025; Bechini and Chandrasekar, 2017; Yin et al., 2021), grounded in the temporal advection assumption, estimate the motion field of radar echoes and extrapolate observed information into missing regions to recover incomplete radar data. This approach can effectively preserve echo structures and temporal consistency when radar echo evolution is relatively smooth and missing regions are spatially continuous. However, under conditions of rapidly developing strong convection or large-scale continuous data gaps, the advection assumption tends to break down, leading to limited reconstruction accuracy. Gao et al. (2021) proposed a deep neural network, CNN-BiConvLSTM, which integrates convolutional neural networks (CNN) with bidirectional convolutional long short-term memory (BiConvLSTM). By adopting a random masking strategy during training, the model can adapt to various missing patterns and reconstruct radar image sequences for missing region recovery. Gong et al. (2023) introduced a UNet-based model (DSA-UNet) that combines dilated convolution with a self-attention mechanism to improve the completion of missing weather radar data. Experimental results demonstrate superior performance in reconstructing extreme reflectivity values and local-scale radar echoes. Compared with traditional statistical methods and deep learning models such as UNet++ GAN (Geiss and Hardin, 2021), this approach reduces prediction bias and enhances reconstruction accuracy. Furthermore, Zhang et al. (2025) proposed an Integrated Restoration Diffusion Model (CIDM), which leverages prior information from known regions as guidance to achieve weather radar data reconstruction under multiple missing scenarios. The method demonstrates significant accuracy improvements in extreme missing conditions, effectively alleviates over-smoothing, and does not require complex data preprocessing.

https://doi.org/10.5194/egusphere-2026-1422
Preprint. Discussion started: 11 May 2026

Although existing methods have made certain progress in the reconstruction of missing radar echoes, they still have limitations (Meuer et al., 2025; He et al.,2025; Liu et al., 2023). On one hand, approaches based on physical constraints or temporal advection assumptions have limited adaptability to complex nonlinear evolution and multi-pattern missing fields. On the other hand, deep learning methods, while possessing strong modeling capabilities, largely rely on known missing masks, which are difficult to obtain in practical radar mosaic data, especially when the spatial distribution of missing regions is highly uncertain. This restricts their generalization and application in operational meteorological services. Therefore, achieving robust reconstruction of missing radar echoes without relying on explicit prior conditions remains a problem that urgently needs to be addressed.

To overcome the limitations of current radar echo reconstruction techniques, which in practical scenarios often depend on missing-data masks and exhibit limited adaptability to diverse and complex missing patterns, this study introduces a reconstruction method that operates without explicit missing-data priors, building upon the technical ideas of CNN-BiConvLSTM and CIDM. Namely, a BiConvLSTM unit (Gao et al., 2021; Chang and Luo, 2019; Liu et al., 2017) is incorporated within an encoder-decoder architecture to form a BiConvLSTM-UNet network, which facilitates bidirectional temporal modeling of radar echo sequences and thus comprehensively captures their spatiotemporal evolution and structural features. Specifically, a loss function tailored for multiple missing data patterns, which integrates diverse missingness constraints during model training to improve the robustness of reconstructions under various missing conditions. During both training and inference, the model operates without relying on missing masks, autonomously reconstructing incomplete regions through learned spatiotemporal dynamics of radar echoes. Moreover, as the model conducts holistic reconstruction of radar echo sequences, a post-processing strategy is implemented at the output stage to refine the reconstruction results and minimize extraneous perturbations to the original, non-missing observations.

The organization of this paper is as follows: Section 2 describes the data sources, preprocessing procedures, and dataset construction; Section 3 details the model architecture, loss function, evaluation metrics, and post-processing approach; Section 4 presents the experimental results and corresponding evaluations; and Section 5 concludes with a summary of the findings, along with a discussion of the study’s limitations and outstanding issues.

2 Data processing

2.1 Data source

The radar reflectivity data used in this study were obtained from composite reflectivity mosaic products (MCR) generated by the operational Severe Weather Automatic Nowcasting (SWAN) system operated by the Hubei

https://doi.org/10.5194/egusphere-2026-1422
Preprint. Discussion started: 11 May 2026

Meteorological Observatory. These radar mosaic products are derived from nine S-band weather radars deployed across Hubei Province, with a spatial resolution of 1 km and a temporal resolution of 6 minutes. The dataset encompasses radar observations from March to September in both 2022 and 2023, covering two successive years and capturing the evolutionary features of radar echoes associated with distinct weather systems during the principal rainy season in Hubei Province, amounting to a total of 102,720 frames. To facilitate efficient model training, the study area is delineated as a 400 × 400 km region centered on Wuhan City in Hubei Province, spanning 112.42–116.42°E and 28.72–32.72°N. The geographic extent of the study area and a representative example of radar mosaic reflectivity data are presented in Fig. 1.

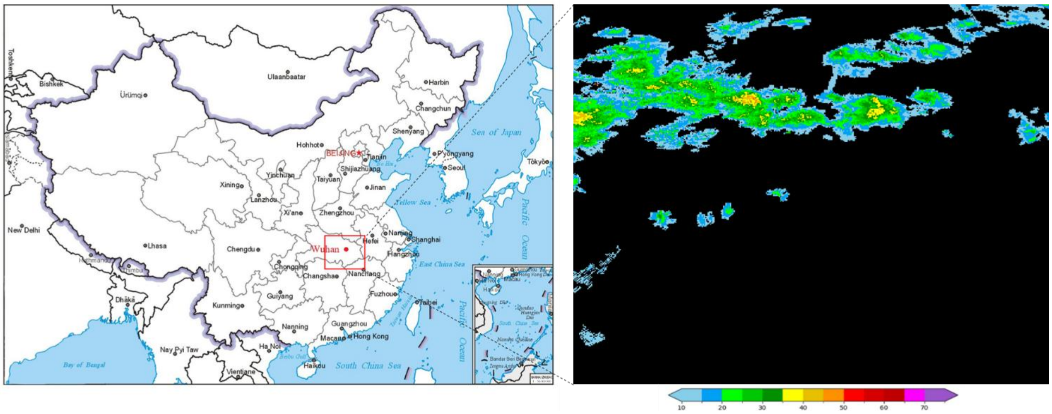

Figure 1 Study area (left) and an example of radar mosaic reflectivity (right).

2.2 Data preprocessing

To establish a valid dataset, the following data preprocessing steps were performed:

First, numerical processing was applied to the radar reflectivity data. This study is restricted to radar echoes associated with substantial precipitation (10–75 dBZ). Accordingly, all values below 10 dBZ were set to 0 dBZ, while those exceeding 75 dBZ were truncated at 75 dBZ. This procedure also provides a basis for subsequent min–max normalization.

Second, appropriate training data were selected. As this study focuses on reconstructing radar echo sequences to fill data gaps, the choice of radar data and sequence length substantially influences experimental outcomes. To prioritize the restoration of missing radar echoes, datasets containing significant echo signals were emphasized. Frames devoid of radar echoes or with minimal coverage—specifically, those in which echo grid points constituted less than 5% of the total grid—were excluded. Additionally, small isolated echoes and noise, defined as contiguous echo regions comprising fewer than 20 grid points, were set to 0 dBZ. Furthermore, from a temporal modeling standpoint, it is essential to

https://doi.org/10.5194/egusphere-2026-1422
Preprint. Discussion started: 11 May 2026

determine a suitable number of consecutive frames per sample to effectively utilize the dynamic evolution of radar echoes for plausible reconstruction of missing areas. To reconcile practical constraints with model training efficiency, three sequence lengths—5, 15, and 30 frames per sample—were evaluated.

For 5-frame sequences, despite the advantages of higher training efficiency and a larger dataset size, the limited information content within each individual sample increases the difficulty of reconstruction learning in the presence of missing data. However, for 30-frame sequences, although they encapsulate substantial temporal dynamics in radar echoes, the considerable data volume per sample presents considerable challenges to training efficiency, dataset scalability, and hardware constraints. Ultimately, a sequence length of 15 frames per sample was identified as optimal, achieving a balance between informational richness, computational efficiency, and hardware limitations.

Following the aforementioned data preprocessing, the final raw dataset comprised 60,615 frames of radar reflectivity data. A subset of 32,115 frames, spanning March to September 2023, served as the training set for model development. For the purpose of guiding learning rate adjustments, implementing early stopping, and selecting optimal model weights during training, 12,990 frames from March to May 2022 were allocated as the validation set. An independent validation set of 4,755 frames from September 2022 was utilized to assess the model's proficiency in reconstructing missing regions and to optimize hyperparameters, including loss function weights. Finally, 10,755 frames from June to August 2022 were designated as the test set for the subsequent quantitative evaluation of experimental results.

2.3 Constructing the loss dataset

The radar mosaic data are generated by integrating observations from multiple weather radars situated at distinct geographical locations at approximately the same time. In the event of system failure, data delay, or data loss affecting any of these radars, the corresponding coverage area will exhibit missing data. To accurately simulate such data loss scenarios, a masking procedure was designed in this study. Specifically, each frame of radar reflectivity data was partitioned into five sectors: upper-left, lower-left, upper-right, lower-right, and central, with each sector spanning a 200×200 grid. Upon selection of a sector for masking, a subregion of dimensions 100×100, 150×150, or 200×200 grid points was defined within it, and all radar reflectivity values inside this subregion were set to 0 dBZ (Fig. 2).

It is important to note that during the construction of the loss dataset, both the selection of the loss region and the dimensions of the loss subregion were randomized for each radar echo sample; however, within individual samples, these parameters remained consistent. When employing subregion sizes of 100×100 or 150×150, all frames from the same sample utilized identical dimensions, while the precise location of the subregion was still randomized, as illustrated in

Fig. 2. This methodology was implemented to thoroughly simulate a wide range of missing-data conditions. Furthermore, to simulate unforeseen circumstances, 1–3 frames per sample were randomly subjected to data loss, ensuring that the model could robustly reconstruct missing regions regardless of which frames were affected and whether the losses occurred consecutively. Using this approach, a corresponding loss dataset was constructed to serve as a foundational resource for subsequent model training.

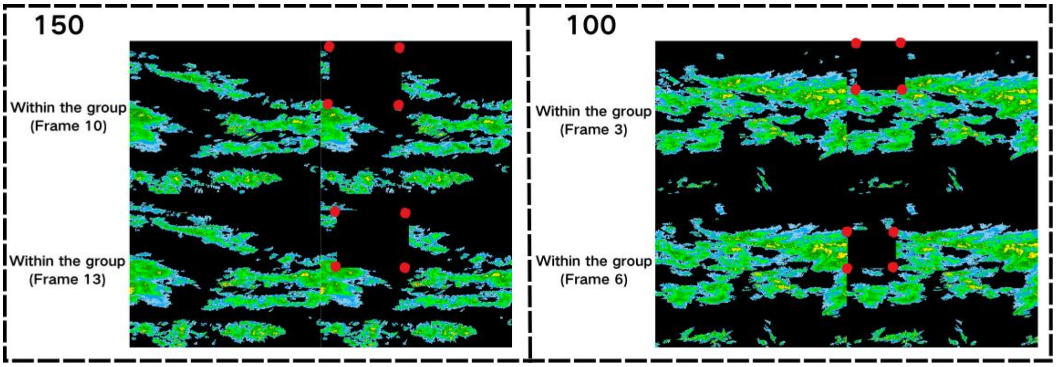

Figure 2 Schematic diagram of random selection of missing intervals (150×150 and 100×100 respectively).

3 Model and methods

3.1 Research question

In operational practice, radar mosaic data can suffer from localized gaps in observation within their nominal coverage areas, owing to issues such as radar hardware malfunctions and delays in data transmission. These gaps typically manifest as spatially contiguous regions and persist across successive time steps, significantly compromising the spatiotemporal continuity of radar echo evolution. Consequently, the accuracy of subsequent quantitative precipitation estimation and nowcasting of severe convective weather events is adversely impacted. As illustrated in Fig. 3, while the complete radar observations (Fig. 3c) show full coverage, the mosaic from the preceding time step (Fig. 3b) exhibits a distinct absence of radar echo in the lower-left sector. In contrast, the mosaic from two-time steps earlier (Fig. 3a) covers an even more limited area, with extensive data loss evident in both the upper-left and lower-left regions.

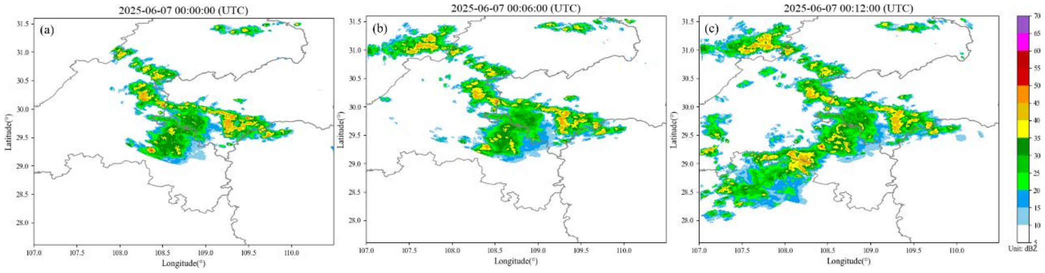

Figure 3 Schematic diagram of radar echo missing in consecutive radar mosaic frames.

From a temporal modeling standpoint, this study regards the problem of restoring missing radar echoes as a sequence reconstruction task. The complete radar echo sequence is defined as:

$$\boldsymbol{Y} = \{\boldsymbol{Y}_{t-T+1}, \dots, \boldsymbol{Y}_{t-1}, \boldsymbol{Y}_t\}, \boldsymbol{Y}_t \in \boldsymbol{R}^{H\times W} \quad (1)$$

where $\boldsymbol{R}$ denotes the complete dataset, while $\boldsymbol{H}$ and $\boldsymbol{W}$ represent the spatial dimensions of the radar mosaics, both set to 400 grid points in this study.

In contrast to conventional restoration techniques that depend on explicit missing masks to guide the reconstruction process, the present study does not presuppose knowledge of the spatial locations of missing regions during training, inference, or post-processing. Instead, the recovery of missing radar echoes is consistently framed as a sequence reconstruction task. It is important to emphasize that the post-processing procedure does not entail additional reconstruction; rather, it serves to constrain and refine the model's output, minimizing potential artifacts in non-missing areas. By learning both the temporal dynamics and spatial structure of radar echo sequences, the model reconstructs the degraded sequence $\widetilde{X}$, thereby restoring missing regions through an implicit modeling approach. The target output of the model is defined as:

$$\widehat{\boldsymbol{Y}}_{t-T+1:t} = \boldsymbol{f}(\widetilde{\boldsymbol{X}}_{t-T+1:t}) \quad (2)$$

Here, $\boldsymbol{f(\cdot)}$ represents the sequence reconstruction model, $\widehat{\boldsymbol{Y}}$ denotes the reconstruction result, and $\widetilde{\boldsymbol{X}}$ denotes the radar echo sequence in which some frames have missing data.

The proposed problem formulation enables the reconstruction of missing radar echoes by incorporating constraints such as overall sequence consistency, and, without requiring prior annotations of the missing areas, establishes a foundation for subsequent model design and application in complex missing-data environments.

3.2 BiConvLSTM-UNet model

In response to the aforementioned research problem, we present a sequence reconstruction model—termed BiConvLSTM-UNet (see Appendix A for detailed architecture)—designed for the restoration of missing data in radar echo sequences. The model accepts a corrupted radar echo sequence ($\widetilde{X}$) as input and reconstructs the data by jointly capturing spatiotemporal evolution patterns and structural features inherent in radar echoes, thereby recovering missing information. Although the model's output spans the entire spatial domain, its optimization objective focuses not on reconstructing non-missing regions, but on inferring missing content under constraints that enforce overall sequence consistency.

As illustrated in Fig. 4, the BiConvLSTM-UNet model employs a U-Net architecture comprising three principal components: an encoder, a bottleneck, and a decoder. The encoder incorporates three cascaded depthwise separable convolution modules (IR-Blocks). To preserve local spatial structures during initial feature extraction, the first layer omits downsampling. Subsequent IR-Blocks progressively reduce spatial resolution by setting the stride of the depthwise convolution to 2, thereby expanding the effective receptive field and increasing channel dimensionality. This process facilitates the construction of hierarchical spatial feature representations, establishing a robust foundation for sequence reconstruction. The bottleneck processes high-level features from the final IR-Block of the encoder, further refining them through an additional IR-Block. A BiConvLSTM module is then applied to perform bidirectional temporal modeling on the feature sequence. By concatenating forward and backward outputs along the feature dimension, the model integrates contextual information, capturing the dynamic evolution of radar echoes across the sequence and improving the representation of temporal continuity and evolutionary trends.

The decoder utilizes an upsampling module based on depthwise separable convolution and PixelShuffle (Qin et al., 2020), referred to as the PS-Block. This module first reconstructs spatial resolution through pixel rearrangement, followed by reorganization of the upsampled features across both spatial and channel dimensions via depthwise separable convolution (Howard et al., 2017). Skip connections are then employed to integrate corresponding encoder-derived features, with subsequent refinement through IR-Blocks to combine high-level semantics and low-level spatial details. This procedure is iteratively applied to progressively restore spatial resolution. Finally, an output normalization module (P_C2D) employs pointwise convolution to project the decoded features, while the ReLU1 activation constrains outputs to the interval [0, 1], ensuring numerical validity and physical interpretability of the reconstructed radar echo sequences. The formulation of ReLU1 is given as follows:

$$f(x)=\min(\max(0,x),1) \tag{3}$$

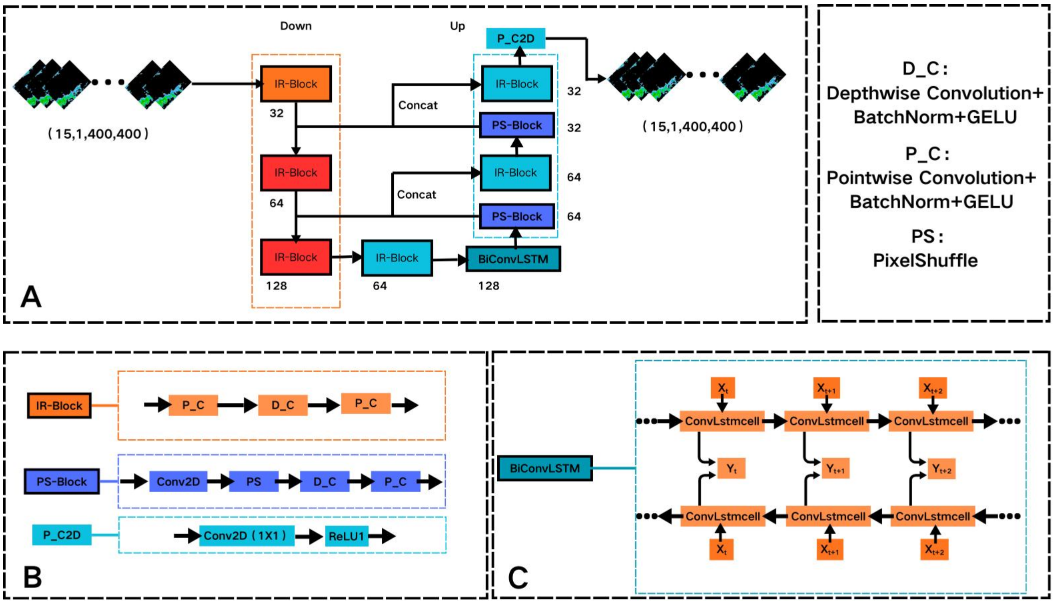

Figure 4 Structure diagram of the BiConvLSTM-UNet model

In the absence of prior knowledge regarding missing regions, the BiConvLSTM-UNet model achieves end-to-end reconstruction of incomplete radar echo sequences by jointly modeling temporal and spatial correlations, thereby enabling spatiotemporally consistent radar echo reconstruction.

3.3 Loss function

In this study, the model training employs a hybrid loss function combining weighted L1 loss and Multi-Scale Structural Similarity (MS-SSIM) loss, which jointly constrains the reconstruction of radar echo sequences by enforcing both pixel-wise accuracy and structural fidelity. The weighted L1 loss is specifically utilized to ensure that reconstructed radar reflectivity values closely approximate the ground truth at the pixel level. To enhance the model's attention to regions of intense radar echoes, a pixel-wise weighting scheme ($\boldsymbol{w}$) is adopted, where the weight increases proportionally with the echo intensity—i.e., stronger reflectivity factors (Z_H) are assigned larger weights (Table 1). These weight values, determined empirically, aim to capture the relative significance of varying echo intensities in the reconstruction task, rather than representing rigorously optimized parameters.

Table 1 The relationship between pixel weights and radar echo intensity.

Z_H (dBZ)	≥10	≥20	≥30	≥40	≥50	≥70
W	1	2	3	5	10	15

https://doi.org/10.5194/egusphere-2026-1422
Preprint. Discussion started: 11 May 2026

The weighted L1 loss is defined as:

$$\mathcal{L}_{WL1} = \frac{1}{N}\sum_{i=1}^{N} w_i \left|Y_i - \hat{Y}_i\right| \tag{4}$$

where N represents the total number of pixels in the sequence, Y_i denotes the ground-truth value of the i-th pixel in the complete radar echo sequence, $\hat{Y}_i$ is the reconstructed value of the i-th pixel in the reconstructed radar echo sequence, and W_i is the weight assigned to the i-th pixel. As the weighted L1 loss is computed across the entire radar echo sequence during training, pixels in non-missing regions are continuously engaged in the supervision process with non-zero weights, thereby imposing effective constraints on the model outputs. Consequently, without the introduction of an explicit mask, the model is capable of both minimizing unnecessary alterations in non-missing regions and directing its focus toward learning the reconstruction of pixels in missing regions.

The MS-SSIM loss enforces constraints on reconstructed radar echoes from a multi-scale structural perspective, thereby ensuring consistency in both global morphology and local textural details. This loss function effectively captures the spatial continuity and hierarchical characteristics inherent in radar echo structures. The MS-SSIM loss is formulated as follows:

$$\mathcal{L}_{MS-SSIM} = 1 - \frac{1}{T}\sum_{j=1}^{T} MS-SSIM(Y_j, \hat{Y}_j) \tag{5}$$

where T represents the total number of frames in a radar echo sequence, Y_j corresponds to the ground-truth radar echo data of the j-th frame, and $\hat{Y}_j$ denotes the reconstructed radar echo data of the j-th frame.

In summary, the combined loss function is defined as:

$$\mathcal{L} = \lambda_1 \mathcal{L}_{\mathrm{WL1}} + \lambda_2 \mathcal{L}_{\mathrm{MS-SSIM}} \tag{6}$$

where λ_1 and λ_2 represent the weighting coefficients for the weighted L1 loss and the MS-SSIM loss, respectively. These two loss components operate in a complementary manner, with the weighted L1 loss managing pixel-level accuracy and the MS-SSIM loss enforcing structural consistency across multiple scales (Zhao et al., 2016). The integration of both terms ensures that the reconstruction of missing regions in radar echo data maintains high numerical precision as well as spatially coherent structural integrity.

3.4 Training configuration

The experimental setup utilized a Python 3.10 environment with the PyTorch 2.6.0 framework and CUDA 12.4. Model training was carried out on two NVIDIA A100 GPUs with a batch size of 2, over a maximum of 200 epochs. Optimization was performed using the Adam optimizer with an initial learning rate of 1×10⁻⁴.

During the training process, a learning rate scheduling strategy was implemented, wherein the Structural Similarity Index (SSIM) metric, evaluated on the full validation sequence, served as the reference. The learning rate was halved whenever the improvement in validation SSIM failed to exceed a threshold of 1×10⁻⁴ relative to the historical optimum for five consecutive epochs, with a minimum learning rate constraint set at 1×10⁻⁶.

To mitigate overfitting and enhance training efficiency, an early stopping criterion was implemented. Specifically, training was halted if the SSIM on the validation set exhibited no substantial improvement—defined as an increase greater than 1×10⁻⁴—for a patience threshold of 10 consecutive epochs, or if the learning rate had decayed to its predefined minimum (1×10⁻⁶). Early stopping was, however, disabled during the initial 30-epoch warm-up phase.

The training employs a combined loss function incorporating weighted L1 and MS-SSIM, which constrains the reconstructed outputs of the model in terms of both pixel-wise accuracy and structural fidelity. The loss weights (λ_1 and λ_2) were optimized through a grid search over a predefined range. The final configuration, with $\lambda_1 = 3$ and $\lambda_2 = 3$, achieves an optimal trade-off between training stability and reconstruction quality.

3.5 Evaluation indicators

1. PSNR (Peak Signal-to-Noise Ratio): Used to quantify pixel-level discrepancies between reconstructed and complete radar echo data, with higher values signifying superior numerical reconstruction fidelity. It is calculated as follows:

$$PSNR = 10 \cdot log_{10}(\frac{(MAX)^2}{MSE}) \tag{7}$$

where MAX denotes the maximum radar reflectivity factor (set to 75 dBZ in this study and normalized to unity), and MSE represents the mean squared error.

2. SSIM (Structural Similarity Index): Quantifies the morphological consistency between reconstructed and ground-truth radar echoes from the perspectives of structure, texture, and contrast. Values range from −1 to 1, with 1 indicating perfect structural similarity. It is defined as:

$$SSIM(\widehat{Y}, Y) = \frac{(2\mu_{\widehat{Y}}\mu_Y + C_1)(2\sigma_{\widehat{Y}Y} + C_2)}{(\mu_{\widehat{Y}}^2 + \mu_Y^2 + C_1)(\sigma_{\widehat{Y}}^2 + \sigma_Y^2 + C_2)} \tag{8}$$

where $\mu_{\widehat{Y}}$ and μ_Y denote the local means of the reconstructed and ground-truth radar echoes, respectively; $\sigma_{\widehat{Y}}^2$ and σ_Y^2 represent their respective variances; $\sigma_{\widehat{Y}Y}$ is their covariance; and C_1 and C_2 are small constants introduced to stabilize the denominator when both numerator and denominator approach zero.

3. POD (Probability of Detection): Measures the proportion of observed strong radar echo events that are correctly reconstructed by the model. A higher POD value indicates a lower miss rate. It is defined as:

https://doi.org/10.5194/egusphere-2026-1422
Preprint. Discussion started: 11 May 2026

$$POD = \frac{TP}{TP + FN} \tag{9}$$

4. FAR (False Alarm Ratio): Quantifies the fraction of reconstructed strong echo regions that are not verified by observations. A lower FAR indicates greater specificity in detecting actual strong echoes, reflecting fewer false alarms. It is calculated as:

$$FAR = \frac{FP}{TP + FP} \tag{10}$$

5. CSI (Critical Success Index): Evaluates the overall accuracy of strong echo reconstruction by jointly accounting for hits, misses, and false alarms. Values range from 0 to 1, with higher values indicating greater spatial agreement between reconstructed and observed strong echo regions. It is defined as:

$$CSI = \frac{TP}{TP + FN + FP} \tag{11}$$

where TP (True Positives) denotes pixels where strong echoes are both observed and correctly reconstructed; FN (False Negatives) denotes pixels where strong echoes are observed but missed in reconstruction; and FP (False Positives) denotes pixels where strong echoes are absent in observations but erroneously reconstructed.

3.6 Post-processing

Since the BiConvLSTM-UNet model reconstructs the entire radar echo sequence—including both missing and non-missing regions—its reconstruction may inadvertently alter originally observed (i.e., non-missing) echo structures. To mitigate this undesirable propagation of reconstruction artifacts into reliable observational data, a targeted post-processing step is applied at the model output stage. Specifically, it selectively preserves the original non-missing echo values from the input (lossy) radar data while replacing only the missing regions with the model’s predictions. This strategy ensures fidelity to observed evidence in intact areas, minimizes spurious modifications outside missing zones, and thereby enhances the physical plausibility and spatial consistency of the final reconstructed sequence. The post-processing operation is formulated as:

$$Y^{post}(i,j) = \begin{cases} \hat{Y}(i,j) & \text{if } \tilde{X}(i,j) = 0 \text{ and } \hat{Y}(i,j) \neq 0, \\ \tilde{X}(i,j) & \text{otherwise} \end{cases} \tag{12}$$

where $Y^{post}(i,j)$ denotes the final post-processed radar echo value at pixel (i, j); $\tilde{X}(i,j)$ denotes the corresponding value from the input (lossy) radar echo data; $\hat{Y}(i,j)$ denotes the model’s reconstructed radar echo value at the same location; and (i,j) indexes the spatial coordinates in the two-dimensional radar echo grid.

4 Experimental Evaluation

4.1 Ablation Experiments

https://doi.org/10.5194/egusphere-2026-1422
Preprint. Discussion started: 11 May 2026

This study addresses missing radar echo regions through sequence-level reconstruction. To systematically isolate and evaluate the contributions of the BiConvLSTM module and the composite loss function to reconstruction performance, we conduct controlled ablation experiments (Table 2). All ablated variants retain the identical backbone architecture, data split (training/validation/test), optimization configuration (optimizer, learning rate schedule, batch size), and inference protocol—ensuring that observed performance differences arise solely from the targeted component modifications. Specifically, Scheme 4 substitutes the bidirectional ConvLSTM with a unidirectional ConvLSTM to assess the impact of temporal context integration in both forward and backward directions; Schemes 2 and 3 respectively remove the weighted L1 term and the MS-SSIM term from the loss function, enabling quantitative attribution of each loss component's role in preserving radar echo morphology and dynamic coherence.

Quantitative evaluation of reconstruction performance within missing radar echo regions is conducted at three reflectivity thresholds: 20 dBZ, 30 dBZ, and 40 dBZ — corresponding to light, moderate, and strong precipitation regimes, respectively. Pixel-level fidelity is assessed using PSNR and SSIM, computed exclusively over masked missing regions to isolate reconstruction accuracy and structural preservation (Zhang et al., 2026). Event-based detection capability is evaluated using CSI, POD, and FAR, all calculated on binary masks derived from the missing-region reconstructions and ground-truth observations — thereby quantifying the model's ability to correctly recover echo presence/absence across different intensity levels (Zhao et al., 2024). For all metrics: ↑ denotes higher-is-better; ↓ denotes lower-is-better.

Table 2 Results of ablation experiments.

	Module	Scheme			
	BiConvLSTM	√	√	√	×
	MS-SSIM Loss	√	√	×	√
	Weighted L1 Loss	√	×	√	√
Threshold	Metrics	**1**	**2**	**3**	**4**
	PSNR↑	**25.608**	25.600	24.445	24.627
	SSIM↑	0.765	**0.769**	0.741	0.734
≥20 dBZ	CSI↑	**0.523**	0.503	0.485	0.451
	POD↑	0.627	0.584	**0.722**	0.540
	FAR↓	0.267	0.222	0.381	**0.190**
≥30 dBZ	CSI↑	**0.379**	0.350	0.375	0.318
	POD↑	0.547	0.449	**0.579**	0.398
	FAR↓	0.315	0.285	0.348	**0.241**
≥40 dBZ	CSI↑	**0.192**	0.136	0.078	0.118
	POD↑	**0.359**	0.175	0.090	0.149
	FAR↓	0.430	0.327	**0.243**	0.282

As shown in Table 2, Scheme 1 achieves either the best or second-best performance across most evaluation metrics, demonstrating that the BiConvLSTM architecture and the adopted loss function jointly contribute to effective reconstruction of missing radar echo regions. A direct comparison between Scheme 1 (with BiConvLSTM) and Scheme 4 (without BiConvLSTM) reveals consistent improvements in both CSI and POD, particularly for strong echoes (≥30 dBZ and ≥40 dBZ). These gains indicate that bidirectional temporal modeling enables more comprehensive utilization of contextual information from both preceding and succeeding frames—thereby enhancing the fidelity and physical plausibility of reconstructed radar echo structures.

From the perspective of the loss function, removing the MS-SSIM loss (Scheme 3) leads to substantial declines in both PSNR and SSIM—dropping from 25.608 to 24.445 and from 0.765 to 0.741, respectively—demonstrating that this term is essential for preserving spatial structural fidelity in reconstructed missing regions. Moreover, for strong radar echoes (≥40 dBZ), Scheme 3 exhibits marked performance degradation relative to the full model (Scheme 1), with CSI and POD falling to 0.078 and 0.090, respectively. This underscores that accurate recovery of intense radar echo structures critically relies on explicit structural regularization; in its absence, morphological coherence deteriorates significantly. In contrast, eliminating the weighted L1 loss (Scheme 2) yields only marginal reductions in PSNR and SSIM. Nevertheless, a direct comparison between Scheme 1 and Scheme 2 reveals a consistent weakening in echo intensity preservation across all intensity thresholds, accompanied by measurable declines in both CSI and POD. These results indicate that the weighted L1 loss effectively constrains pixel-wise intensity deviation, mitigates over-smoothing of radar echo amplitudes, and thereby enhances quantitative and perceptual reconstruction quality in missing regions.

It should be noted that, across all echo intensity thresholds, Scheme 1 achieves relatively high CSI and POD values—but at the cost of a moderately elevated FAR. This trade-off suggests that the scheme prioritizes recall-oriented reconstruction: by recovering plausible echo signals in missing regions, it effectively reduces missed detections; however, this sensitivity also leads to an increased incidence of false alarms.

The ablation study demonstrates that the BiConvLSTM module significantly improves temporal modeling capability; meanwhile, the MS-SSIM loss and weighted L1 loss serve complementary functions—MS-SSIM enforces structural consistency, whereas the weighted L1 loss preserves echo intensity fidelity—thereby jointly enhancing the model's performance in reconstructing missing radar echo regions.

4.2 Comparative experiments

To further verify the BiConvLSTM-UNet model's capability in reconstructing missing radar echo regions, we conducted a comparative evaluation against other advanced deep learning approaches—specifically ConvLSTM (Shi et al., 2015) and DSA-UNet (Gong et al., 2023)—as well as a classical motion-based method, optical flow (Ayzel et al., 2019). All models are trained and evaluated under identical experimental conditions—including the same dataset, preprocessing procedure, and evaluation metrics—to ensure methodological fairness and result comparability.

Table 3 Comparative performance evaluation of different models.

Threshold	Metrics	Model			
		BiConvLSTM-Unet	ConvLSTM	DSA-Unet	Optical Flow
	PSNR↑	**25.608**	24.638	24.464	23.707
	SSIM↑	**0.765**	0.747	0.738	0.688
≥20 dBZ	CSI↑	**0.523**	0.418	0.416	0.442
	POD↑	**0.627**	0.432	0.532	0.561
	FAR↓	0.267	**0.044**	0.218	0.379
≥30 dBZ	CSI↑	**0.379**	0.317	0.263	0.297
	POD↑	**0.547**	0.339	0.389	0.403
	FAR↓	0.315	**0.086**	0.297	0.503
≥40 dBZ	CSI↑	**0.192**	0.148	0.110	0.142
	POD↑	**0.359**	0.160	0.178	0.201
	FAR↓	0.430	**0.093**	0.282	0.599

As can be seen in Table 3, the ConvLSTM model achieves the lowest FAR across all reflectivity thresholds—demonstrating its superior capability in false alarm suppression. Its PSNR, SSIM, and CSI scores rank immediately below those of BiConvLSTM-UNet, with negligible inter-metric disparity, indicating robust and balanced performance in missing radar echo reconstruction. However, qualitative analysis in Fig. 5 reveals a consistent limitation: ConvLSTM struggles to reconstruct sharp, spatially coherent boundaries in missing echo regions, resulting in locally unsmooth structural transitions and diminished spatial continuity.

https://doi.org/10.5194/egusphere-2026-1422
Preprint. Discussion started: 11 May 2026

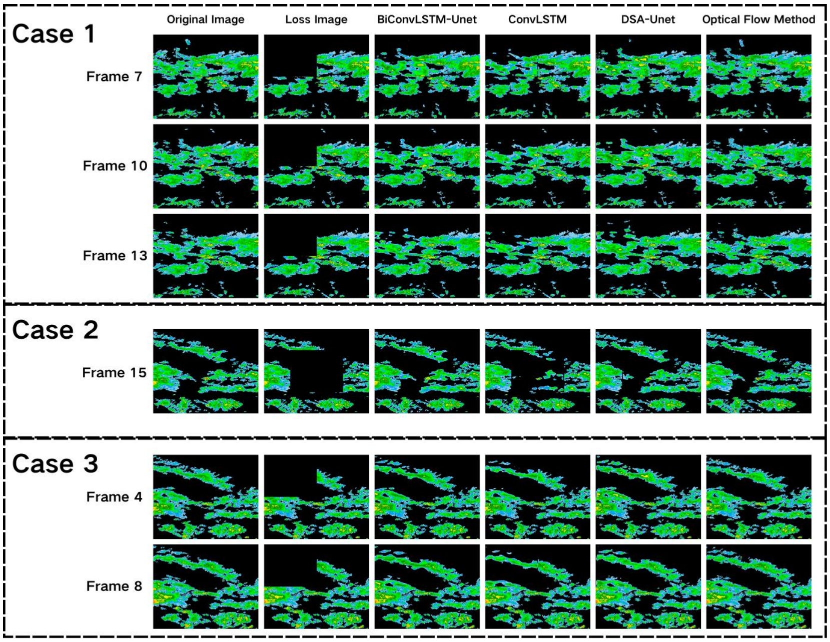

Figure 5 Comparison of radar echo restoration results of various models in different cases.

DSA-UNet achieved high POD values across all models, reflecting its strong capability in proactively recovering valid radar echoes. Qualitative analysis in the example results (Fig. 5) further demonstrates that, relative to BiConvLSTM-UNet, DSA-UNet delivers more complete and spatially coherent reconstruction in partially missing echo regions—yielding visually plausible outputs. However, boundary reconstruction remains a limitation: DSA-UNet tends to produce over-smoothed transitions and loss of fine-scale echo morphology, particularly at region edges. Its relatively high FAR further suggests a tendency toward echo overestimation under ambiguous or low-signal conditions. In contrast, the optical flow method better preserves the spatial morphology and structural integrity of radar echo boundaries in reconstructed regions, resulting in subjectively realistic visual outputs. Yet, as a purely motion-based extrapolation technique, it inherently assumes echo translation and approximate intensity conservation—assumptions that fail to account for physical processes such as echo genesis, dissipation, or intensity modulation during temporal evolution. Consequently, optical flow consistently underperforms on quantitative metrics—including PSNR, SSIM, and CSI—with degradation most severe in rapidly evolving convective systems where non-translational dynamics dominate.

Quantitative evaluation and qualitative analysis jointly demonstrate that BiConvLSTM-UNet achieves superior overall performance across key metrics—including PSNR, SSIM, CSI, and POD—and exhibits enhanced fidelity in reconstructing the structural boundaries of missing radar echo regions. However, its elevated FAR reveals a consistent tendency toward echo overestimation, particularly in low-reflectivity or spatially ambiguous areas.

https://doi.org/10.5194/egusphere-2026-1422
Preprint. Discussion started: 11 May 2026

4.3 Analysis of the impact of non-missing regions

BiConvLSTM-UNet performs holistic reconstruction of missing radar echo sequences—a strategy that, while effective for gap filling, may inadvertently perturb pixel values in non-missing regions. To quantify this side effect and rigorously assess the efficacy of post-processing in preserving structural consistency within observed (i.e., non-missing) echo regions, we restrict analysis exclusively to frames containing missing data. Within these frames, we conduct a pixel-wise comparative evaluation between the raw model outputs and the corresponding post-processed results—specifically within the non-missing regions (Table 4). Root Mean Square Error (RMSE) and Mean Absolute Error (MAE) serve as complementary metrics: RMSE emphasizes sensitivity to localized outliers and large-magnitude deviations, thereby highlighting instances of severe inconsistency; MAE provides a robust measure of average deviation across all non-missing pixels, reflecting global fidelity and stability (Chai and Draxler, 2014). The definitions are as follows:

$$\boldsymbol{RMSE}=\sqrt{\frac{\sum_{i,j}\boldsymbol{M}_{i,j}\left(\boldsymbol{Y}_{i,j}\text{-}\hat{\boldsymbol{y}}_{i,j}\right)^{2}}{\sum_{i,j}\boldsymbol{M}_{i,j}}} \tag{13}$$

$$\boldsymbol{MAE}=\frac{\sum_{i,j}\boldsymbol{M}_{i,j}\left|\boldsymbol{Y}_{i,j}\text{-}\hat{\boldsymbol{y}}_{i,j}\right|}{\sum_{i,j}\boldsymbol{M}_{i,j}} \tag{14}$$

Here, $\boldsymbol{Y}_{i,j}$ denotes the observed radar echo intensity (in dBZ), $\hat{\boldsymbol{y}}_{i,j}$ represents the model-predicted echo value—either from raw reconstruction or post-processed output—and the binary mask ($\boldsymbol{M}_{i,j}$) indicates data availability: $\boldsymbol{M}_{i,j}$=1 for non-missing (observed) regions and $\boldsymbol{M}_{i,j}$=0 for missing regions.

Table 4 Evaluation of post-processing effects in non-missing regions of radar echo data.

	RMSE	MAE
Reconstruction results	0.704	0.260
Post-processing results	0.266	0.013

The results in Table 4 show that, the model’s holistic reconstruction yields RMSE and MAE values of 0.704 and 0.260, respectively, within non-missing regions—indicating unintended distortion of valid radar echo data. Upon integrating the proposed post-processing strategy, these metrics decline substantially to 0.266 (RMSE) and 0.013 (MAE), reflecting a marked reduction in spurious modifications to non-missing regions. Crucially, this improvement is achieved without compromising reconstruction accuracy in missing regions. Collectively, these results demonstrate that the post-processing strategy effectively preserves structural fidelity in non-missing regions while maintaining robust reconstruction capability in missing regions.

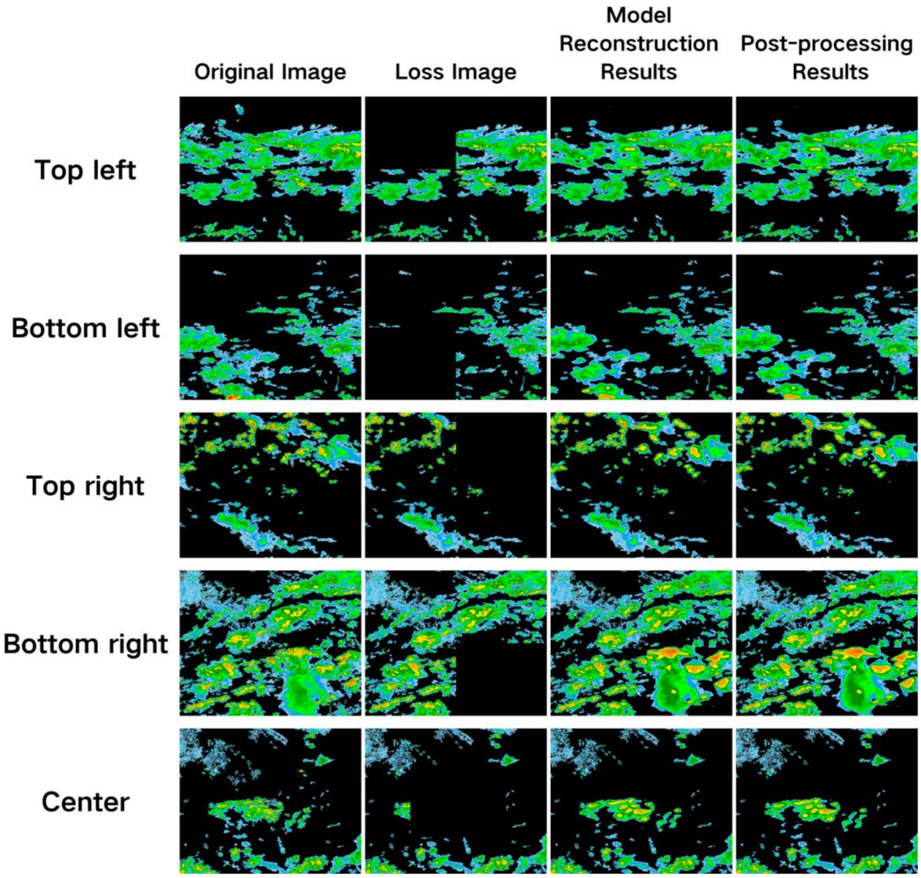

Figure 6 Comparative analysis of post-processing effects on non-missing regions of radar echo data.

4.4 Model generalization ability test

To evaluate model generalization under variations in missing length and temporal continuity, we designed a controlled experimental protocol comprising distinct training and testing regimes. During training, missing patterns were sampled at random across 1–3 frames—thereby jointly simulating both isolated (non-contiguous) and brief contiguous gaps. During testing, two targeted scenarios were introduced: (i) random 4-frame missing (preserving temporal dispersion) and (ii) consecutive 4-frame missing (enforcing maximal temporal continuity)—to systematically probe reconstruction robustness under extended gap duration and heightened structural discontinuity. Critically, the 1–3 frame missing patterns used in this evaluation were freshly regenerated—decoupled from those employed in ablation and comparative experiments—to ensure independent assessment and mitigate confounding bias in generalization performance.

Table 5 Model generalization performance on radar echo missing regions.

Threshold	Metrics	Option			
		Random 1-3 Frames	Sequential 1-3 Frames	Random 4 Frames	Sequential 4 Frames
	PSNR↑	25.991	25.475	25.485	24.353
	SSIM↑	0.751	0.744	0.734	0.728
≥20 dBZ	CSI↑	0.505	0.421	0.482	0.385
	POD↑	0.602	0.499	0.573	0.447
	FAR↓	0.253	0.206	0.240	0.214
≥30 dBZ	CSI↑	0.361	0.300	0.303	0.252
	POD↑	0.516	0.424	0.444	0.354
	FAR↓	0.295	0.273	0.315	0.285
≥40 dBZ	CSI↑	0.161	0.124	0.112	0.105
	POD↑	0.304	0.198	0.230	0.169
	FAR↓	0.394	0.318	0.322	0.309

As presented in Table 5, extending the random missing length from 1–3 frames to 4 frames induces only marginal declines in PSNR and SSIM for the BiConvLSTM-UNet model, confirming its robustness to modest increases in missing duration. In contrast, CSI and POD exhibit more pronounced degradation — particularly under intense radar echo thresholds (≥30 dBZ and ≥40 dBZ)—while FAR remains stable or even decreases across several thresholds. This pattern suggests that the model preserves detection specificity under extended random gaps, albeit with reduced sensitivity to strong echoes. Under consecutive 4-frame missing, however, all metrics—PSNR, SSIM, CSI, and POD—show consistent and statistically meaningful deterioration across reflectivity thresholds, indicating that uninterrupted temporal context loss fundamentally impairs the model's capacity to recover spatiotemporal coherence in radar echo fields. Notably, FAR continues to decrease, reflecting a conservative reconstruction bias: the model increasingly favors omission over false activation when deprived of contiguous temporal cues—a behavior that trades recall for precision under severe structural uncertainty.

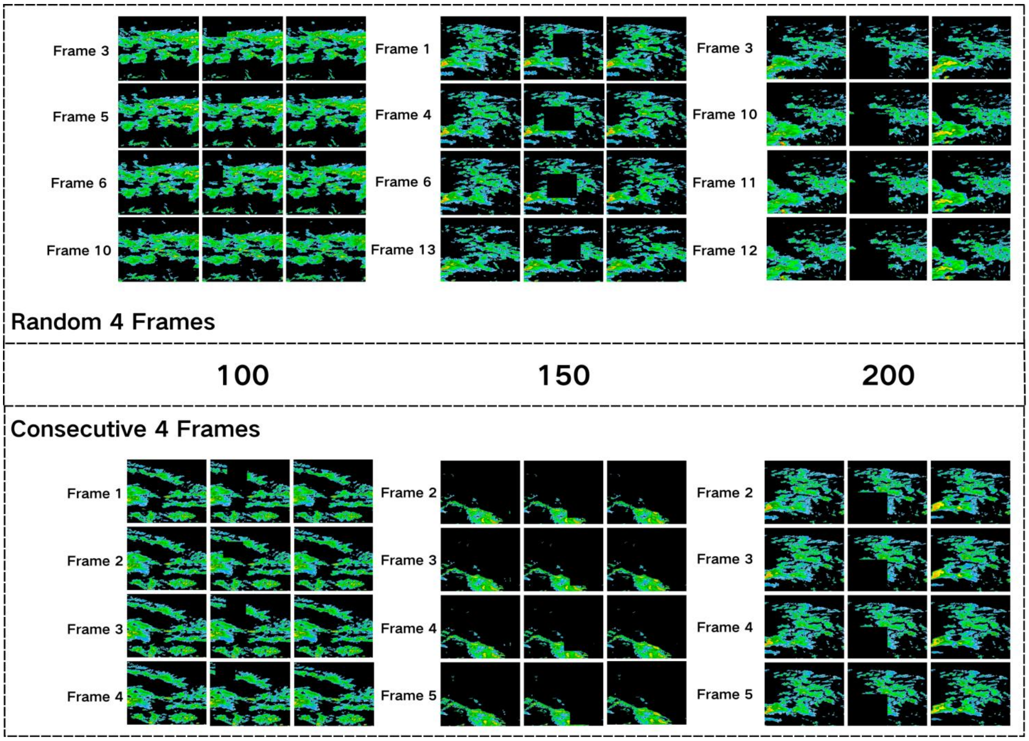

Figure 7 Example diagram for testing the generalization ability of the BiConvLSTM-UNet model.

As shown in Fig. 7, the BiConvLSTM-UNet model maintains robust reconstruction performance across varying missing patterns—specifically, under both extended missing length and reduced temporal continuity—indicating substantive generalization capability. Nevertheless, performance degrades systematically with increasing missing intensity: under random 4-frame missing, metrics decline modestly; under consecutive 4-frame missing, however, all evaluation metrics (PSNR, SSIM, CSI, POD) exhibit pronounced and consistent deterioration. This graded, interpretable degradation—monotonic with respect to missing severity and qualitatively aligned with the underlying spatiotemporal modeling assumptions—further validates the model's behavior as physically plausible and methodologically sound.

5 Summary and Discussion

Partial radar echo missing—frequently observed in operational weather radar mosaics—represents a fundamental limitation to their reliability and quantitative utility in real-time forecasting and warning systems. Conventional restoration methods, whether rooted in radar meteorological physics or statistical interpolation, exhibit diminished effectiveness under dynamically complex weather conditions and struggles to characterize the nonlinear spatiotemporal evolution inherent to convective precipitation echoes. Classical optical flow approaches reconstruct missing data by

https://doi.org/10.5194/egusphere-2026-1422
Preprint. Discussion started: 11 May 2026

estimating echo motion fields; however, they critically depend on the brightness constancy and small-motion continuity assumptions—conditions routinely violated during rapid storm development, merging, or abrupt intensity changes—leading to significant instability and reconstruction artifacts. In recent years, deep learning methods have been increasingly adopted for radar missing-data reconstruction; however, prevailing approaches typically require explicit missing masks as auxiliary inputs and exhibit strong sensitivity to missing pattern configurations—resulting in limited robustness when confronted with unseen, irregular, or structurally heterogeneous missing scenarios. To address these constraints, this study proposes BiConvLSTM-UNet: a sequence-to-sequence reconstruction model grounded in an end-to-end, mask-free paradigm. Built upon a U-Net backbone, the architecture incorporates bidirectional ConvLSTM units at the bottleneck layer to explicitly model temporal dependencies across feature sequences. By intrinsically encoding the spatiotemporal continuity and dynamic evolution priors of radar echo sequences—without reliance on external mask supervision—the model achieves implicit identification and physically consistent reconstruction of missing regions.

An experimental dataset was constructed under multiple missing-data configurations to enable systematic model training and comprehensive performance evaluation. Quantitative results demonstrate that BiConvLSTM-UNet consistently outperforms both the conventional optical flow method and representative deep learning models—including ConvLSTM and DSA-UNet—across four key metrics: PSNR, SSIM, CSI, and POD. Case studies further reveal that BiConvLSTM-UNet robustly preserves boundary sharpness and spatial continuity in reconstructed radar echo regions, accurately recovering dominant morphological structures without requiring explicit missingness masks. Notably, while model performance gradually degrades with increasing echo missingness, it retains measurable adaptability; however, intensity overestimation emerges in certain high-missingness scenarios. This suggests that pixel-level intensity fidelity and false alarm suppression remain critical avenues for future refinement.

Overall, this study demonstrates the feasibility and effectiveness of reconstructing radar missing regions through spatiotemporal sequence modeling—without requiring explicit missing masks—thereby establishing a novel technical pathway to reduce model reliance on prior knowledge of missing patterns and improve reconstruction robustness across diverse missing scenarios. Notably, mask-free training introduces nontrivial challenges in both convergence stability and hyperparameter sensitivity. Future work should therefore focus on two complementary directions: first, refining model architecture (e.g., via attention-gated feature modulation) to enhance fidelity in missing-region reconstruction; second, designing loss formulations that mitigate the dominance of non-missing pixels—without resorting to binary masks—such as by incorporating spatially adaptive weighting or uncertainty-guided pixel selection.

Appendices

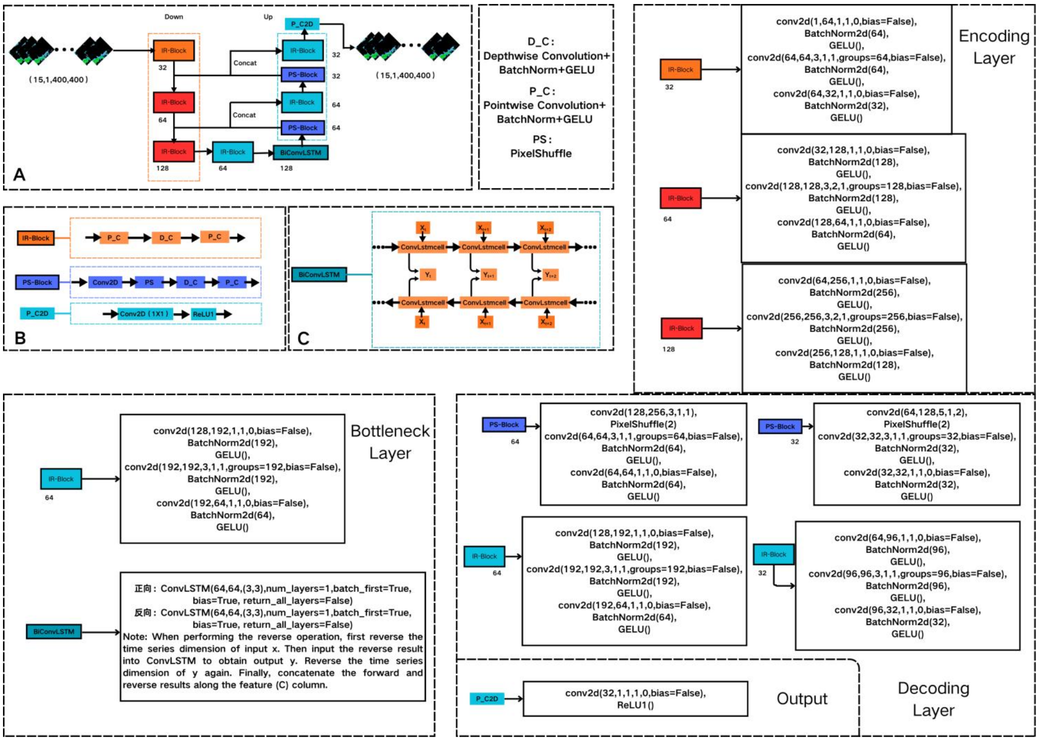

```
conv2d(1,64,1,1,0,bias=False),
BatchNorm2d(64),
GELU(),
conv2d(64,64,3,1,1,groups=64,bias=False),
BatchNorm2d(64),
GELU(),
conv2d(64,32,1,1,0,bias=False),
BatchNorm2d(32),
GELU()
```

```
conv2d(32,128,1,1,0,bias=False),
BatchNorm2d(128),
GELU(),
conv2d(128,128,3,2,1,groups=128,bias=False),
BatchNorm2d(128),
GELU(),
conv2d(128,64,1,1,0,bias=False),
BatchNorm2d(64),
GELU()
```

```
conv2d(64,256,1,1,0,bias=False),
BatchNorm2d(256),
GELU(),
conv2d(256,256,3,2,1,groups=256,bias=False),
BatchNorm2d(256),
GELU(),
conv2d(256,128,1,1,0,bias=False),
BatchNorm2d(128),
GELU()
```

```
conv2d(128,192,1,1,0,bias=False),
BatchNorm2d(192),
GELU(),
conv2d(192,192,3,1,1,groups=192,bias=False),
BatchNorm2d(192),
GELU(),
conv2d(192,64,1,1,0,bias=False),
BatchNorm2d(64),
GELU()
```

```
正向：ConvLSTM(64,64,(3,3),num_layers=1,batch_first=True,
bias=True, return_all_layers=False)
反向：ConvLSTM(64,64,(3,3),num_layers=1,batch_first=True,
bias=True, return_all_layers=False)
```

Note: When performing the reverse operation, first reverse the time series dimension of input x. Then input the reverse result into ConvLSTM to obtain output y. Reverse the time series dimension of y again. Finally, concatenate the forward and reverse results along the feature (C) column.

```
conv2d(128,256,3,1,1),
PixelShuffle(2)
conv2d(64,64,3,1,1,groups=64,bias=False),
BatchNorm2d(64),
GELU(),
conv2d(64,64,1,1,0,bias=False),
BatchNorm2d(64),
GELU()
```

```
conv2d(64,128,5,1,2),
PixelShuffle(2)
conv2d(32,32,3,1,1,groups=32,bias=False),
BatchNorm2d(32),
GELU(),
conv2d(32,32,1,1,0,bias=False),
BatchNorm2d(32),
GELU()
```

```
conv2d(128,192,1,1,0,bias=False),
BatchNorm2d(192),
GELU(),
conv2d(192,192,3,1,1,groups=192,bias=False),
BatchNorm2d(192),
GELU(),
conv2d(192,64,1,1,0,bias=False),
BatchNorm2d(64),
GELU()
```

```
conv2d(64,96,1,1,0,bias=False),
BatchNorm2d(96),
GELU(),
conv2d(96,96,3,1,1,groups=96,bias=False),
BatchNorm2d(96),
GELU(),
conv2d(96,32,1,1,0,bias=False),
BatchNorm2d(32),
GELU()
```

```
conv2d(32,1,1,1,0,bias=False),
ReLU1()
```

Figure 8 Schematic diagram of BiConvLSTM-UNet model structure and parameters.

Data availability

The data for this research can be obtained directly from the author, Husong Guo, via email at 17737491980@163.com.

Author contributions

Husong Guo: Investigation, Methodology, Data curation, Visualization, Formal analysis, Writing (original draft preparation). **Muyun Du**: Conceptualization, Methodology, Supervision, Data curation, Visualization, Funding acquisition, Writing (review and editing). **Xiangyu Fan**: Supervision, Funding acquisition. **Cuihong Wu**: Supervision, Validation. **Anwei Lai:** Validation. **Hedi Ma**: Visualization.

Competing interests

The authors declare that they have no conflict of interest.

Financial support

This research is jointly supported by the National Natural Science Foundation of China (Grant 42575172, 42230612, 42005121), the Joint Fund of Hubei Province Natural Science Foundation (Grant 2023AFD095), Open Fund of Heavy Rainfall Research of China (Grant BYKJ2024Z08, BYKJ2025M18) and the Innovation and Development Project of China Meteorological Administration (Grant CXFZ2024J015).

References

Ayzel, G., Heistermann, M., and Winterrath, T.: Optical flow models as an open benchmark for radar-based precipitation nowcasting (rainymotion v0.1), Geosci. Model Dev., 12, 1387–1402, https://doi.org/10.5194/gmd-12-1387-2019, 2019.

Bechini, R. and Chandrasekar, V.: An enhanced optical flow technique for radar nowcasting of precipitation and winds, Journal of Atmospheric and Oceanic Technology, 34, 2637–2658, https://doi.org/10.1175/JTECH-D-17-0110.1, 2017.

Chai, T. and Draxler, R. R.: Root mean square error (RMSE) or mean absolute error (MAE)? – Arguments against avoiding RMSE in the literature, Geosci. Model Dev., 7, 1247–1250, https://doi.org/10.5194/gmd-7-1247-2014, 2014.

Chang, Y. and Luo, B.: Bidirectional convolutional LSTM neural network for remote sensing image super-resolution, Remote Sensing, 11, 2333, https://doi.org/10.3390/rs11202333, 2019.

Esbrí, L., Rigo, T., Llasat, M. C., Biondi, R., Federico, S., Gluchshenko, O., Kerschbaum, M., Lagasio, M., Mazzarella, V., and Milelli, M.: Application of severe weather nowcasting to case studies in air traffic management, Atmosphere, 14, 1238, https://doi.org/10.3390/atmos14081238, 2023.

Fabry, F.: Radar meteorology: principles and practice, Cambridge University Press, https://doi.org/10.1017/CBO9781107707405, 2015.

Forcadell, V., Augros, C., Caumont, O., Dedieu, K., Ouradou, M., David, C., Figueras i Ventura, J., Laurantin, O., and Al-Sakka, H.: Severe-hail detection with C-band dual-polarization radars using convolutional neural networks, Atmos. Meas. Tech., 17, 6707–6734, https://doi.org/10.5194/amt-17-6707-2024, 2024.

Gou, Y. and Chen, H.: Combining radar attenuation and partial beam blockage corrections for improved quantitative application, Journal of Hydrometeorology, 22, 139–153, https://doi.org/10.1175/JHM-D-20-0121.1, 2021.

Gong, A., Chen, H., and Ni, G.: Improving the completion of weather radar missing data with deep learning, Remote Sensing, 15, 4568, https://doi.org/10.3390/rs15184568, 2023.

Geiss, A. and Hardin, J. C.: Inpainting radar missing data regions with deep learning, Atmos. Meas. Tech., 14, 7729–7747, https://doi.org/10.5194/amt-14-7729-2021, 2021.

Gao, L., Zheng, Y., Wang, Y., Xia, J., Chen, X., Li, B., Luo, M., and Guo, Y.: Reconstruction of missing data in weather radar image sequences using deep neuron networks, Applied Sciences, 11, 1491, https://doi.org/10.3390/app11041491, 2021.

Howard, A. G., Zhu, M., Chen, B., Kalenichenko, D., Wang, W., Weyand, T., Andreetto, M., and Adam, H.: Mobilenets: Efficient convolutional neural networks for mobile vision applications, arXiv preprint arXiv:1704.04861, https://doi.org/10.48550/arXiv.1704.04861, 2017.

He, X., Zhou, Z., Zhang, W., Zhao, X., Chen, H., Chen, S., and Bai, L.: Diffsr: Learning radar reflectivity synthesis via diffusion model from satellite observations, ICASSP 2025-2025 IEEE International Conference on Acoustics, Speech and Signal Processing (ICASSP), 1–5, 10.1109/ICASSP49660.2025.10888161, 2025.

Liu, Q., Sun, J., Zhang, Y., and Liu, X.: DenMerD: a feature enhanced approach to radar beam blockage correction with edge-cloud computing, Journal of Cloud Computing, 13, 32, https://doi.org/10.1186/s13677-024-00607-x, 2024.

Li, Z., Wu, C., Liu, L., Zhang, Y., and Chen, C.: Three-dimensional mosaic method of dual-polarization parameters for a high-density radar network, Atmospheric Research, 108494, https://doi.org/10.1016/j.atmosres.2025.108494, 2025.

Liu, Q., Yang, Z., Ji, R., Zhang, Y., Bilal, M., Liu, X., Vimal, S., and Xu, X.: Deep vision in analysis and recognition of radar data: Achievements, advancements, and challenges, IEEE Systems, Man, and Cybernetics Magazine, 9, 4–12, 10.1109/MSMC.2022.3216943, 2023.

Liu, Q., Zhou, F., Hang, R., and Yuan, X.: Bidirectional-convolutional LSTM based spectral-spatial feature learning for hyperspectral image classification, Remote Sensing, 9, 1330, https://doi.org/10.3390/rs9121330, 2017.

Meuer, J., Bouwer, L. M., Kaspar, F., Lehmann, R., Karl, W., Ludwig, T., and Kadow, C.: Infilling of missing rainfall radar data with a memory-assisted deep learning approach, Hydrol. Earth Syst. Sci., 29, 3687–3701, https://doi.org/10.5194/hess-29-3687-2025, 2025.

Peng, D., Chen, M., Zhang, Y., and Tian, Z.: Enhanced optic-flow extrapolation for Doppler radar nowcasting with dynamic weight attention, Expert Systems with Applications, 267, 126168, https://doi.org/10.1016/j.eswa.2024.126168, 2025.

Qin, M., Mavromatis, S., Hu, L., Zhang, F., Liu, R., Sequeira, J., and Du, Z.: Remote sensing single-image resolution improvement using a deep gradient-aware network with image-specific enhancement, Remote Sensing, 12, 758, https://doi.org/10.3390/rs12050758, 2020.

Shi, X., Chen, Z., Wang, H., Yeung, D.-Y., Wong, W.-K., and Woo, W.-c.: Convolutional LSTM network: A machine learning approach for precipitation nowcasting, Advances in neural information processing systems, 28, https://doi.org/10.48550/arXiv.1506.04214, 2015.

Saltikoff, E., Haase, G., Delobbe, L., Gaussiat, N., Martet, M., Idziorek, D., Leijnse, H., Novák, P., Lukach, M., and Stephan, K.: OPERA the radar project, Atmosphere, 10, 320, https://doi.org/10.3390/atmos10060320, 2019.

Yao, M., Du, M. Y., Yu, R., Jiang, X. L., Ma, H. D., Tang, G. Y., and Liu, P. T.: Deep learning-based object detection of electromagnetic interference echoes from weather radar data, J. Meteor. Res., 40, 287–300, https://doi.org/10.1007/s13351-026-5107-8, 2026.

Yin, J., Gao, Z., and Han, W.: Application of a radar echo extrapolation-based deep learning method in strong convection nowcasting, Earth and Space Science, 8, e2020EA001621, https://doi.org/10.1029/2020EA001621, 2021.

Yin, X., Hu, Z., Zheng, J., Zuo, Y., Huang, F., and Zhu, Y.: Using deep learning to fill in dual-polarization radar echoes occlusions, Journal of Applied Meteorology, 33, 581–593, 10.11898/1001-7313.20220506, 2022.

Zhang, M., Chen, Y., Yang, F., and Qin, Z.: Attention-driven and multi-scale feature integrated approach for earth surface temperature data reconstruction, Geosci. Model Dev., 19, 73–91, https://doi.org/10.5194/gmd-19-73-2026, 2026.

Zhao, Z., Duan, C., Song, L., Zhang, Q., Zhu, W., and Liu, Y.: MissPred: A robust two-stage radar echo extrapolation algorithm for incomplete sequences, Remote Sensing, 17, 2066, https://doi.org/10.3390/rs17122066, 2025.

Zhao, H., Gallo, O., Frosio, I., and Kautz, J.: Loss functions for image restoration with neural networks, IEEE Transactions on computational imaging, 3, 47–57, 10.1109/TCI.2016.2644865, 2016.

Zhao, J., Tan, J., Chen, S., Huang, Q., Gao, L., Li, Y., and Wei, C.: Intelligent reconstruction of radar composite reflectivity based on satellite observations and deep learning, Remote Sensing, 16, 275, https://doi.org/10.3390/rs16020275, 2024.

Zhang, W., Zhang, X., Dong, J., Song, X., and Pang, R.: CIDM: A comprehensive inpainting diffusion model for missing weather radar data with knowledge guidance, ISPRS Journal of Photogrammetry and Remote Sensing, 221, 299–309, https://doi.org/10.1016/j.isprsjprs.2025.02.001, 2025.

Zhang, P., Zrnić, D., and Ryzhkov, A.: Partial beam blockage correction using polarimetric radar measurements, Journal of Atmospheric and Oceanic Technology, 30, 861–872, https://doi.org/10.1175/JTECH-D-12-00075.1, 2013.